Time scales for pluton growth, magma chamber formation and super-eruptions

M.E. van Zalinge[1], D.F. Mark[2,3], R.S.J. Sparks[1], Tremblay, M.M.[4], C.B. Keller[5], F.J. Cooper[1] and A. Rust[1]

1. School of Earth Sciences, University of Bristol, Wills Memorial Building, Bristol BS8 1RJ, United Kingdom.
2. Scottish Universities Environmental Research Centre, Rankine Avenue, Scottish Enterprise Technology Park, East Kilbride, G75 0QF, United Kingdom.
3. Department of Earth and Environmental Science, University of St Andrews, St Andrews, KY16 9AJ, UK
4. Department of Earth, Atmospheric and Planetary Sciences, 550 Stadium Mall Drive, Purdue University, West Lafayette, IN 47907-2051, U.S.A.
5. Department of Earth Sciences, Dartmouth College, Hanover, NH 03755, U.S.A.

(Word count main text: 2384)

Summary

Generation of silicic magmas leads to emplacement of granite plutons, huge explosive volcanic eruptions and physical and chemical zoning of continental and arc crust[1-7]. While time scales for silicic magma generation in the deep and middle crust are prolonged[8], magma transfer into the upper crust followed by eruption is episodic and can be rapid[9-12]. Ages of inherited zircons and sanidines from four Miocene ignimbrites in the Central Andes indicate a gap of 4.6

Myr between initiation of pluton emplacement in the upper crust and onset of super-eruptions, with a 1 Myr cyclicity. Here we show that inherited zircons and sanidine crystals were stored at temperatures $<470^{o}C$ in these plutons prior to incorporation in ignimbrite magmas. Our observations can be explained by silicic melt segregation in a middle crustal hot zone with episodic melt ascent from an unstable layer at the top of the zone with a time scale governed by the rheology of the upper crust. After thermal incubation of growing plutons, large magma chambers can form in only a few thousand years or less in the upper crust by dyke transport from the hot zone melt layer. Instability and disruption of earlier plutonic rock occurs in a few decades or less just prior to or during super-eruptions.

Large-volume silicic ignimbrites are co-genetic with emplacement of large granitoid plutons in the upper crust[1-5]. Ignimbrites provide snapshots in the evolution of silicic magmatic systems. Information about pluton emplacement, magma chamber formation and magma dynamics that leads to super-eruptions comes from geochronology, petrology and crystal residence time studies[6-12], complemented by numerical modelling[13-17]. Upper crustal silicic igneous systems are part of transcrustal magmatic systems in which differentiated (silicic) melts can be generated in the middle and lower crust by reactive flow in mushes created by long-term influx of basalt[8,19-22]. Buoyancy instabilities[8,23] drive silicic magmas to shallow crustal levels, sometimes resulting in episodic explosive volcanism.

The longevity of plutonic and related volcanic systems (typically 10^6 to 10^7 years)[1-7,17,18] contrasts with short timescales (typically $< 10^3$ years) needed to assemble shallow magma chambers prior to large-magnitude ignimbrite eruptions[9-12,23]. Antecrysts entrained within erupting magmas are stored at temperatures near or below the solidus for long periods prior to eruption[24-26] and commonly have very short residence in host magmas (decades or less).

To understand the onset of pluton emplacement relative to volcanism, the formation of large eruptible magma bodies and the dynamic processes associated with super-eruptions, we integrate geochronology, crystal-diffusion modelling and trans-crustal magma transport modelling. We combine new $^{40}Ar/^{39}Ar$ ages on tens of individual sanidine fragments and laser-ablation (LA)-ICP-MS ages of zircon crystals from early Miocene rhyolitic ignimbrites in northern Chile. These data are combined with existing (re-interpreted) $^{206}Pb/^{238}U$ Chemical Abrasion (CA)-ID-TIMS geochronology of the youngest zircon populations identified by LA-ICP-MS. To interpret these data, we develop an internally-consistent conceptual model with estimates of fluxes and time scales needed to build and maintain an eruptible magma body within a magma reservoir, with considerations of magma supply and making space for pluton growth by ductile deformation of the crust. Terminology for magmatic systems is summarised in methods.

Geological background

The Oxaya Formation, located on the western slope of the Central Andes (Figure 1), comprises four large-volume (collectively > 2000 km^3) regional ignimbrites[27,28]: Poconchile (22.626 +0.053/-0.060 Ma); Cardones (21.840 +0.048/-0.054 Ma); Molinos (20.821 +0.057/-0.068 Ma) and Oxaya (19.553 +0.049/-0.053 Ma). Poconchile, Cardones and Oxaya eruption ages were re-interpreted from van Zalinge et al.[27] by applying a new Bayesian model[66]. The Molinos age is a new $^{40}Ar/^{39}Ar$ analysis of sanidine. The ages are reported at the 95% confidence interval including systematic uncertainties.

The Oxaya ignimbrites are rhyolites with mineral assemblages of plagioclase, quartz, biotite, FeTi oxides, $\pm$ sanidine, $\pm$ amphibole[27,29] and accessory zircon. The Cardones ignimbrite[28] is crystal-rich (ca. 30-40%) and contains two pumice varieties, one with high sanidine content but no amphibole and magma temperatures estimated[29] in the range 770-670^{o}C, and the other with low or no sanidine, minor amphibole and 850-750°C. Barometry, thermometry, and rare earth element geochemistry, indicate that these silicic magmas were generated by differentiation from wet basaltic to andesitic magmas with temperatures of 950-850°C emplaced in the middle and lower crust at depths of approximately 15 km or more[28]. The silicic magmas were then emplaced at depths of 6.0-8.7 $\pm$ 2.0 km[29] prior to eruption. Isotopic data indicate assimilation of older crust[30].

Geochronology of sanidines and inherited zircons

Single-fragment $^{40}Ar/^{39}Ar$ total fusion ages of sanidine crystal fragments and ages determined by LA-ICP-MS spot analyses of inherited zircons reveal highly dispersed age spectra for each ignimbrite, with single-crystal-fragment ages spread over millions of years prior to eruption (Figure 2). While widely documented in zircon[31-33], age dispersion is only recently being recognized in erupted sanidine[26,34].

The sanidine and zircon data indicate a magmatic history extending over 7.7 Myr from the oldest inherited zircons (27.3 Ma) to the eruption age of the youngest ignimbrite (19.6 Ma). The onset of magma system development is at least 4.6 Myr before the first eruption at 22.7 Ma. Observations of lithologies and detrital zircon ages in the late Oligocene to early Miocene Azapa Formation exclude significant silicic volcanism 27.3-22.7 Ma: volcanic clasts are intermediate[35] and only 1 out of 149 detrital zircons[36] falls within 27.3-22.7 Ma. We thus interpret zircon and sanidine ages >22.7 Ma as evidence of pluton growth without associated volcanism. The data suggest zircon and sanidine crystallized in three of the ignimbrites continuously mostly in the 1 Myr interval before eruption, and sanidines retained Ar because of cold storage. Data for Molinos suggest either a hiatus in zircon crystallization 1 Myr prior to eruption, or that the Molinos magma body did not incorporate zircons from this period.

The repose intervals between ignimbrite eruptions (Figure S2) are: 0.80 +0.07/-0.07 Myr for Poconchile-Cardones; 1.02 +0.08/-0.07 Myr for Cardones-Molinos; and 1.28 +0.07/-0.08 Myr for Molinos-Oxaca. The inherited sanidine are qualitatively consistent with the magmatic history implied by the inherited zircons but exhibit a younger and narrower age spread. The percentage of sanidine fragments in each sample older than the eruption ages are: Poconchile (64%); Cardones (60%); Molinos (38%); and Oxaya (45%).

Interpretation of inherited sanidine data

The $^{40}Ar/^{39}Ar$ ages older than eruption ages were likely modified by mixing and diffusion. Sanidine crystals are commonly zoned[29], so the Ar isotopic compositions could be mixtures of old crystal cores and young, eruption-age parts of the crystal resulting in an intermediate age. In between crystallization and eruption, radiogenic ^{40}Ar production is countered by diffusion, which depends exponentially on temperature[37]. We modelled variation of apparent age in sanidine due to diffusive loss of ^{40}Ar as a function of crystal size and temperature to constrain storage temperatures. Diffusive loss of ^{40}Ar from sanidine will create rim-to-core age gradients in individual crystals, with the oldest ages preserved in the cores. Our analyses are typically of 0.5 to 1 mm fragments derived from much larger crystals up to 11 mm wide, so we calculated the ages of crystal cores (Figure 3).

Model results (Figure 3a) indicate that old ages up to several Ma older than the eruption age can be preserved in the cores of large sanidine crystals if the sanidines are stored at temperatures below ~470°C, with the oldest sanidines remaining below 400°C. Previously the concept of cold storage based on zircon geochemistry and geochronology inferred temperatures at or below the solidus of rhyolitic magmatic systems (~700°C)[12,25]. Cold storage can thus occur at temperatures well below the solidus[26].

Preservation of old sanidine ages also indicates short magma residence times because diffusion of ^{40}Ar is fast at magmatic temperatures. We calculated the apparent age of sanidine crystal cores as a function of grain size for temperatures of 700°C and 770°C[29], assuming no prior diffusive ^{40}Ar loss during cold storage. To preserve the range of observed sanidine ages, magma residence times must be years to centuries (Figure 3b). For example, for an original grain diameter of 11 mm, ages older than 26 Ma can be preserved in crystal cores for ~50 years at 700˚C or 7-8 years at 770˚C. These residence times agree with estimates for incorporation of inherited crystals into a magma body before eruption[8-10,12,24]. Some diffusive loss of ^{40}Ar during cold storage and subsequent residence in the magma likely explain a narrower range of sanidine ages than zircon ages.

Sanidine crystals may experience diffusive loss during welding and cooling of an ignimbrite. A temperature of 600°C for 650 years at 200 m depth were estimated for the Cardones ignimbrite[38]. For 11 mm crystal diameters, ages >26 Ma can be preserved in crystal cores for ~10^3 years at 600 ˚C (Figure 3c), demonstrating that post eruption losses of ^{40}Ar are minor.

Discussion

Our conceptual model of magma generation, magma transport, magma chamber formation and onset of super-eruptions (Figure 4) builds on ideas of the dynamics and evolution of transcrustal magma systems[8,20,22]. Here, silicic melt generated by reactive flow segregates continuously and slowly within a growing middle crustal hot zone constructed by incremental intrusion of mafic magma[22]. A layer of buoyant silicic melt accumulates at the top of the hot zone. Rayleigh Taylor instabilities develop[23] that eventually trigger rapid ascent of large volumes of silicic magma into the upper crust, initially forming granite plutons and leading to thermal conditions for magma chamber formation.

The Oxaya magmatic system lasted at least 7.7 Myr, a time comparable to major plutonic episodes and development of large caldera systems[1-7,17,18]. Zircon ages are robust to thermal disturbance, so the absence of age clusters is consistent with continuous zircon crystallization related to upper crustal magma emplacement. However, the low precision of LA-ICP-MS cannot preclude episodic magmatism at time scales < 0.5 Ma[25]. The magmatic history involved an initial ~4.6 Myr stage of pluton growth in the upper crust, followed by ~ 3.1 Myr of episodic ignimbrite eruptions.

We interpret the first stage as the incubation period predicted from thermal models of incremental pluton growth and supported by geological and petrological evidence[13-15,17,18]. Incubation period is defined as the time for the upper crustal magma reservoir to generate a region with a melt fraction exceeding 0.4[14]. During this stage silicic magma is transferred from the middle crust (depths ≥15 km) to the upper crust (depths ~ 5 to 8 km)[29] to form granite plutons. Using equation 7 from Annen et al.[15] and a 1-D approximation we estimate an upper limit for magma reservoir growth of 3.5 mm/yr over 4.6 Myr. We envisage pluton growth by displacement of hot ductile crust downwards and sideways[17] (Figure 4). In incremental growth models each increment of magma cools and crystallizes quickly while most of the growing pluton remains at much lower temperature. Models[13,39] of pluton growth indicate that temperatures below 450ºC can be sustained across the pluton for growth rates of < 1 cm/yr, explaining preservation of old sanidine ages. Lack of silicic volcanic clasts and detrital zircons with early Miocene ages in underlying Azapa sediments[36] suggests that the incubation stage involved only pluton emplacement.

Magma chambers supplied by magma ascent from the hot zone can assemble in the upper crust at the end of the incubation period (Figure 4a). We attribute growth of large chambers as the consequence of highly episodic growth[39,40]. We interpret the inherited sanidine and zircon ages as originating form previously emplaced granite plutons incorporated at a late stage of chamber growth. These plutonic rocks, at temperature well below the solidus, are disrupted and mixed into silicic magma chamber just decades before and during a super-eruption (Figure 4b) .

We apply a model[23] of episodic magma ascent due to laterally-confined Rayleigh Taylor instabilities in slowly developing melt layers at the top of the middle crustal hot zone beneath a subsolidus upper crust with a viscosity μ_c (see methods). Based on this model, we propose that repose periods between major ignimbrite-forming eruptions are dominantly controlled by upper crust rheology. Of interest are the conditions required for the timescale for the instability to grow into a diapir (τ_d) to match the ~1 Myr intervals between the major Oxaya ignimbrites (methods equation M3). For a melt layer width (diameter) of 40 km, and a density contrast between the buoyant melt and the overlying crust of $\Delta\rho$=300 kg/m^3, we calculate that τ_d = 1 Myr requires a crustal viscosity of μ_c = 5 x 10^{19} Pa s, which is consistent with experimental data[41] at 500-700°C. Large repose intervals that allow generation of magma volumes for super-eruptions can be explained by a strong crust and silicic magma accumulation in the middle crust.

We compared dyking and diapirism[42,43] as mechanisms of magma transport (methods) and conclude dyke transport enables rapid formation of upper crustal magma chambers implied by the geochronological and petrological observations. Conditions for dyke formation are inferred to develop at the top of the incipient diapir resulting from Rayleigh Taylor instability growth over a time comparable to τ_d. We develop and justify (methods) a simple exchange flow model[44] of crust with viscosity μ_c slowly subsiding over a large area and magma with viscosity μ_m ascending through a narrow cylindrical conduit as an approximation of dyke transport. Calculations of conduit radii, fluxes, magma chamber volume and assembly time are presented in Table 1 for $\Delta\rho$ = 300 kg/m^3, μ_m = 10^5 Pa s and μ_c = 10^{19} Pa s, considering transfer of magma through the conduit from a layer initially 1 km thick of radius R. Three radius values for the collapsing cylindrical crust region are chosen at 15, 20 and 25 km to span the scale of large plutons and super-eruption caldera systems. Fluxes are large, explaining how large-volume magma chambers can be assembled over periods of a few thousand years.

Thermal models of episodic pluton growth and magma chamber formation[13-15,17,39,40] are consistent with the exchange flow model. Episodic magma ascent at rates much higher than time-averaged rates are needed to form large upper crustal magma chambers[39] and are illustrated by parametric models for the Jurassic Yerington batholith in Nevada[40], which includes the Luhr Hill pluton with similar geochemical and mineralogical characteristics to the Oxaya ignimbrites. Intrusion rates greater than about 10 cm/yr were required to form a large shallow magma chamber. For a cylindrical magma chamber with radius 20 km this translates into 0.12 km^3/yr or more, comparable to the calculated exchange flow fluxes (Table 1) and about two orders of magnitude greater than the 0.001 km^3/yr needed to generate ~1000 km^3 of magma in 1 Myr. Here we explicitly invoke slow extraction of silicic melt from mush in the middle crust. Episodic instability of an accumulating silicic melt layer beneath a high viscosity crust leads to rapid magma transfer into the upper crust (Figure 4).

This study combining zircon and sanidine geochronology, crystal-diffusion modelling and magma transport modelling, highlights the potential of a multifaceted approach to understanding the evolution and dynamics of large magmatic systems. Previous studies of zircon age distributions led to the concept of long periods of cold storage and rapid mobilization of silicic magma into eruptible magma bodies[24]. However, in our study preservation of old sanidines rules out cold storage within a non-eruptible mush system at or above the solidus[25]. Rather the observations indicate catastrophic assimilation and mixing of cold plutonic rock, which we propose occurred just prior to and during eruption (Figure 4b). We applied a Rayleigh Taylor instability model to silicic melt accumulations in the middle crust to explain episodic ignimbrite volcanism where observed repose times of ~1 Myr are controlled by upper crustal rheology. A new model of exchange flow involving magma ascent along dykes and crustal subsidence can explain rapid upper magma chamber assembly sourced from middle crustal mush zones, leading to super-eruptions.

Data Availability

All data related to this manuscript are provided as tables in supplementary materials.

Code Availability

Not applicable

References

1. Lipman, P.W. Incremental assembly and prolonged consolidation of Cordilleran magma chambers: Evidence from the Southern Rocky Mountain volcanic field. Geosphere 3, 42–70, (2007).

2. Glazner, A. F., Bartley, J. M., Coleman, D. S., Gray, W. & Taylor, R. Z. Are plutons assembled over millions of years by amalgamation from small magma chambers? Geological Society of AmericaToday 14, 4-12 (2004).

3. Bachmann, O., Miller, C. & De Silva, S. The volcanic–plutonic connection as a stage for understanding crustal magmatism. Journal of Volcanology and Geothermal Research 167, 1-23 (2007).

4. Frazer, R. E., Coleman, D. S. & Mills, R. D. Zircon U-Pb geochronology of the Mount Givens Granodiorite: Implications for the genesis of large volumes of eruptible magma. Journal of Geophysical Research: Solid Earth 119, 2907-2924 (2014).

5. Lipman, P. W. & Bachmann, O. Ignimbrites to batholiths: Integrating perspectives from geological, geophysical, and geochronological data. Geosphere, GES01091. 01091 (2015).

6. Charlier, B.L.A., Wilson, C.J.N., Lowenstern, B., Blake, S., van Calsteren P.W. & Davidson, J.P. Magma Generation at a Large, Hyperactive Silicic Volcano (Taupo, New Zealand) Revealed by U–Th and U–Pb Systematics in Zircons. J Petrology 46, 3-32 (2005)

7. de Silva, S.L. & Gosnold, W.D. Episodic construction of batholiths: insights from the spatiotemporal development of an ignimbrite flare-up. Journal of Volcanology and Geothermal Research 167, 320–335 (2007).

8. Sparks, R.S.J., Annen, C., Blundy, J.D., Cashman, K.V., Rust, A.C. & Jackson, M.D. Formation and dynamics of magma reservoirs. Philosophical Transactions of the Royal Society A 377: 20180019 (2019).

9. Druitt, T.H., Costa, F., Deloule, E., Dungan, M. & Scaillet, B. (2012). Decadal to monthly timescales of magma transfer and reservoir growth at a caldera volcano. Nature 482, 77–80 (2012).

10. Shamloo, H.I. & Till, C.B. Decadal transition from quiescence to supereruption: petrologic investigation of the Lava Creek Tuff, Yellowstone Caldera. Contributions to Mineralogy and Petrology 174:32 (2019).

11. Pamukçu, A.S., Wright, K.A., Gualda, G.A.R. & Gravley, D. Magma residence and eruption at the Taupo Volcanic Center (Taupo Volcanic Zone, New Zealand): insights from rhyolite-MELTS geobarometry, diffusion chronometry, and crystal textures. Contributions to Mineralogy and Petrology 175:48 (2020).

12. Rubin, A.E., Kari M. Cooper, K.M., Till, C.B., Kent A.R.J., Costa F., Bose M. Gravley D., Deering, C. & Cole J. Rapid cooling and cold storage in a silicic magma reservoir recorded in individual crystals. Science 356, 1154–1156 (2017)

13. Annen, C., Scaillet, B. & Sparks, R.S.J. Thermal constraints on the emplacement rate of a large intrusive complex: the Manaslu Leucogranite, Nepal Himalaya. Journal of Petrology 47, 71-95 (2006).

14. Annen, C. From plutons to magma chambers: thermal constraints on the accumulation of eruptible silicic magma in the upper crust. Earth and Planetary Science Letters 284, 409-416 (2009).

15. Annen, C., Blundy, J. D., Leuthold, J. & Sparks, R. S. J. Construction and evolution of igneous bodies: Towards an integrated perspective of crustal magmatism. Lithos 230, 206-221 (2015).

16. Gregg, P.M., de Silva, S.L., Grosfils, E.B. & Parmigiani, J.P. Catastrophic caldera-forming eruptions: Thermomechanics and implications for eruption triggering and maximum caldera dimensions on Earth. Journal of Volcanology and Geothermal Research 241–242, 1–12 (2012).

17. Paterson, S., Okaya, D., Memeti, V., Economos, R. & Miller R.B. Magma addition and flux calculations of incrementally constructed magma chambers in continental margin arcs: Combined field, geochronologic, and thermal modeling studies. Geosphere 7, 1439-1468 (2011).

18. Walker, B. A., Grunder, A.L. and Wooden J.L. Organisational and thermal maturity of long-lived arc systems: evidence from zircons at the Aucanquilcha volcanic cluster, northern Chile. Geology 38, 1007-1010 (2010).

19. Annen, C., Blundy, J.D. & Sparks, R.S.J. The genesis of intermediate and silicic magmas in deep crustal hot zones. Journal of Petrology 47, 505-539 (2006).

20. Solano, J.M.S., Jackson, M.D., Sparks, R.S.J., Blundy, J.D. & Annen, C. Segregation in Deep Crustal Hot Zones: a Mechanism for Chemical Differentiation, Crustal Assimilation and the Formation of Evolved Magmas. Journal of Petrology 53, 1999-2026 (2012).

21. Cashman K.V., Sparks, R.S.J. & Blundy J. Vertically extensive and unstable crystals mushes: a unifying view of igneous processes associated with volcanoes. Science 355, 6331 eaag3055 (2017).

22. Jackson, M. Blundy J. & Sparks R.S.J. Chemical differentiation, cold storage and remobilization of magma in the Earth's crust. Nature 564, 405-409 (2018).

23. Seropian, G., Rust, A. & Sparks, R.S.J. The gravitational stability of lenses in magma mushes: confined Rayleigh-Taylor instabilities. Journal of Geophysical Research 123, 3593-3607 (2017).

24. Cashman, K.V. & Giordano, G. Calderas and magma reservoirs. Journal of Volcanology and Geothermal Research 288, 28-45 (2014).

25. Cooper. K.M. & Kent, A.J.R. Rapid remobilization of magmatic crystals kept in cold storage. Nature 506, 480-483 (2014).

26. Andersen, N.L., Jicha, B.R., Singer, B.S. & Hildreth, W. Incremental heating of Bishop Tuff sanidine reveals pre-eruptive radiogenic Ar and rapid remobilization from cold storage PNAS 114 (47) 12407-12412 (2017).

27. van Zalinge, M.E., Sparks, R.S.J., Cooper, F.J. & Condon, D. Early Miocene large volume ignimbrites of the Oxaya Formation, Central Andes. Journal of the Geological Society of London 173, 716-733 (2016).

28. García, M., Gardeweg, M., Clavero, J. & Hérail, G. 2004. Arica map: Tarapacá Region, scale

1:250,000. In: CartaGeológica de Chile SerieGeología básica, 84, Servicio Nacional de Geología y Minería, Santiago.

29. van Zalinge, M.E., Sparks, R.S.J. & Blundy, J.D. Petrogenesis of the large-volume Cardones ignimbrite, Chile; development and destabilisation of a complex magma-mush system. Journal of Petrology 58, 1975- 2006 (2018).

30. Freymuth, H., Brandmeier, M. & Wörner, G. The origin and crust/mantle mass balance of Central Andean ignimbrite magmatism constrained by oxygen and strontium isotopes and erupted volumes. Contributions to Mineralogy and Petrology 169, 1-24 (2015).

31. Lissenberg, C. J., Rioux, M., Shimizu, N., Bowring, S. A. & Mével, C. Zircon Dating of Oceanic Crustal Accretion. Science 323, 1048–1050 (2009).

32. Wotzlaw, J.-F. et al. Tracking the evolution of large-volume silicic magma reservoirs from assembly to supereruption. Geology 41, 867–870 (2013).

33. Samperton, K. M., Bell, E. A., Barboni, M., Keller, C. B. & Schoene, B. Zircon age-temperature-compositional spectra in plutonic rocks. Geology 45, 983–986 (2017).

34. Ellis, B. S. et al. Split-grain $^{40}Ar/^{39}Ar$ dating: Integrating temporal and geochemical data from crystal cargoes. Chemical Geology 457, 15–23 (2017).

35. Pinto. L., Hérail, G., Fontan, F. & Parseval, P. Neogene erosion and uplift of the western edge of the Andean Plateau as determined by detrital heavy mineral analysis. Sedimentary Geology 195, 217-237 (2007).

36. Wotzlaw, J.F., Decou, A., von Eynatten, H., Worner, G. & Frei, D. Jurassic to Palaeogene tectono-magmatic evolution of northern Chile and adjacent Bolivia from detrital zircon U-Pb geochronology and heavy mineral provenance. Terra Nova 23, 399–406 (2011)

37. Hora, J. M., Singer, B. S., Jicha, B. R., Beard, B. L., Johnson, C. M., de Silva, S. & Salisbury, M. Volcanic biotite-sanidine ^{40}Ar/^{39}Ar age discordances reflect Ar partitioning and pre-eruption closure in biotite. Geology 38, 923-926 (2010).

38. Platzman, E.S., Sparks, R.S.J. & Cooper, F.J. Fabrics, facies and flow through a large-volume ignimbrite: Pampa De Oxaya, Chile. Bulletin of Volcanology 82:8 (2020).

39. Schöpa, A. & Annen, C. The effects of magma flux variations on the formation and lifetime of large silicic magma chambers. Journal of Geophysical Research: Solid Earth 118, 926-942 (2013).

40. Schöpa A., Annen, C., Dilles, J.H., Sparks R.S.J. & Blundy, J.D. Magma Emplacement Rates and Porphyry Copper Deposits: Thermal Modeling of the Yerington Batholith. Economic Geology 112, 1653-1672 (2018).

41. Burgmann, R. & Dresen, G. Rheology of the Lower Crust and Upper Mantle: Evidence from Rock Mechanics, Geodesy, and Field Observations. Annual Reviews of Earth & Planetary Sciences 36, 531-567 (2008).

42. Burov, E., Jaupart, C. & Guillou-Frottier, L. Ascent and emplacement of buoyant magma bodies in brittle-ductile upper crust. Journal of Geophysical Research: Solid Earth, 108(B4) (2003).

43. Petford, N., Cruden, A.R., McCaffrey, K.J.W. & Vigneresse, J.L. Granite magma formation, transport and emplacement in the Earth's crust. Nature 408, 669–673 (2000).

44. Suckale, J., Qin, Z., Picchi, D., Keller, T., & Battiato, I. (2018). Bistability of buoyancy-driven exchange flows in vertical tubes. Journal of Fluid Mechanics, 850, 525-550.

Crustal radius (km)	Conduit radius (m)	Magma flux (km^3/yr)	Magma volume (km^3)	Assembly time (years)
15	4.7	0.18	710	3800
20	6.3	0.58	1300	2200
25	7.9	1.40	2000	1400

Table 1. Results of calculations for exchange flow. Calculations are shown for the flow up a cylindrical conduit and are rounded to 2 significant figures. Results are shown for conduit radius, magma flux, magma chamber volume and magma chamber assembly times for a melt layer 1 km thick with crustal viscosity $\mu_c = 10^{19}$ Pa s. Calculations for three different radius values of the magma system (See Figure 4) are presented.

Figures

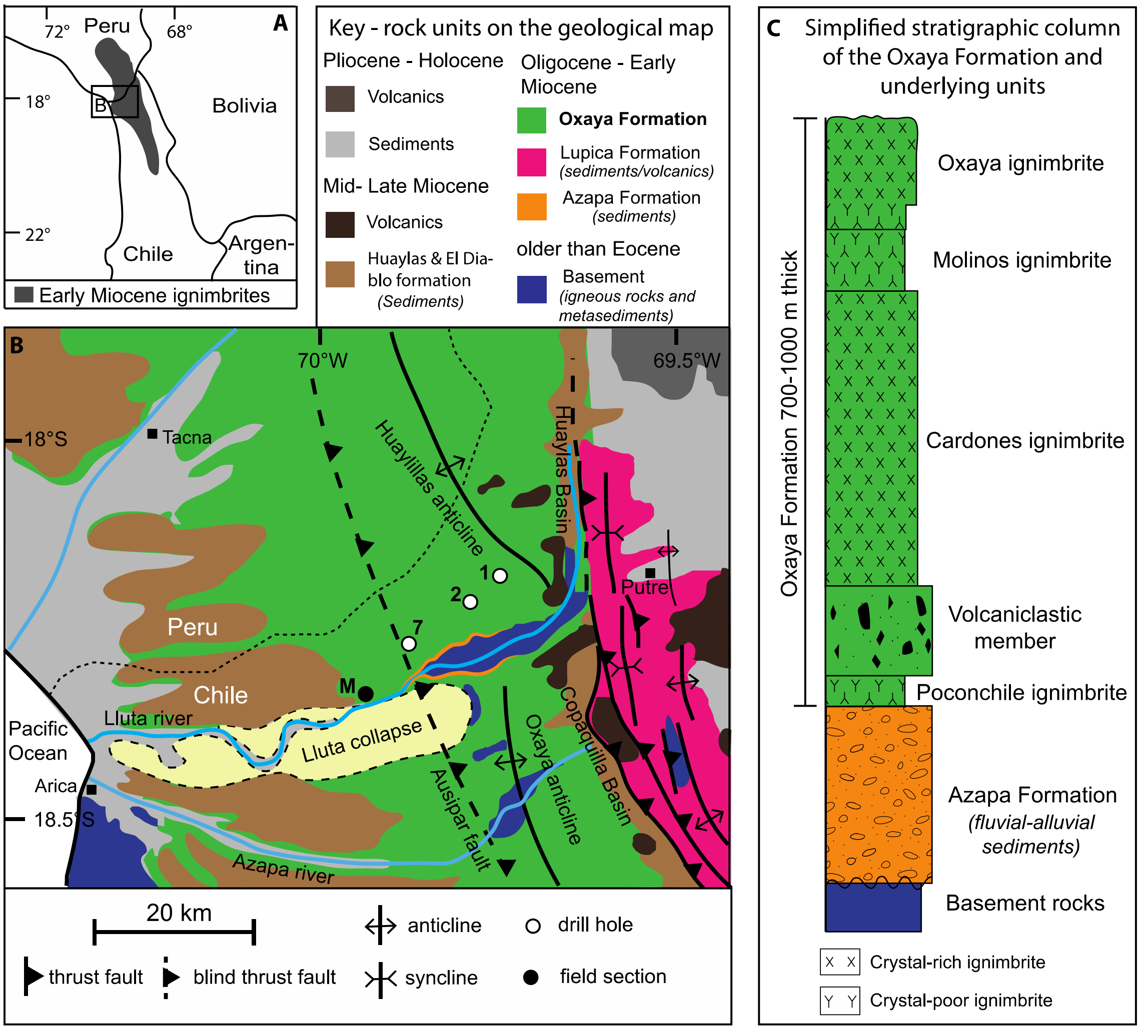

Figure 1. (A) Study area in Central Andes with distribution of early Miocene ignimbrites. (B) Simplified geological map of study area showing distribution of the Oxaya Formation and major structural features in the area modified by van Zalinge et al.[27] after Garcia et al.[28] (C) Simplified stratigraphy[27] of the Oxaya Formation and underlying units based on locality M and drill hole data (B).

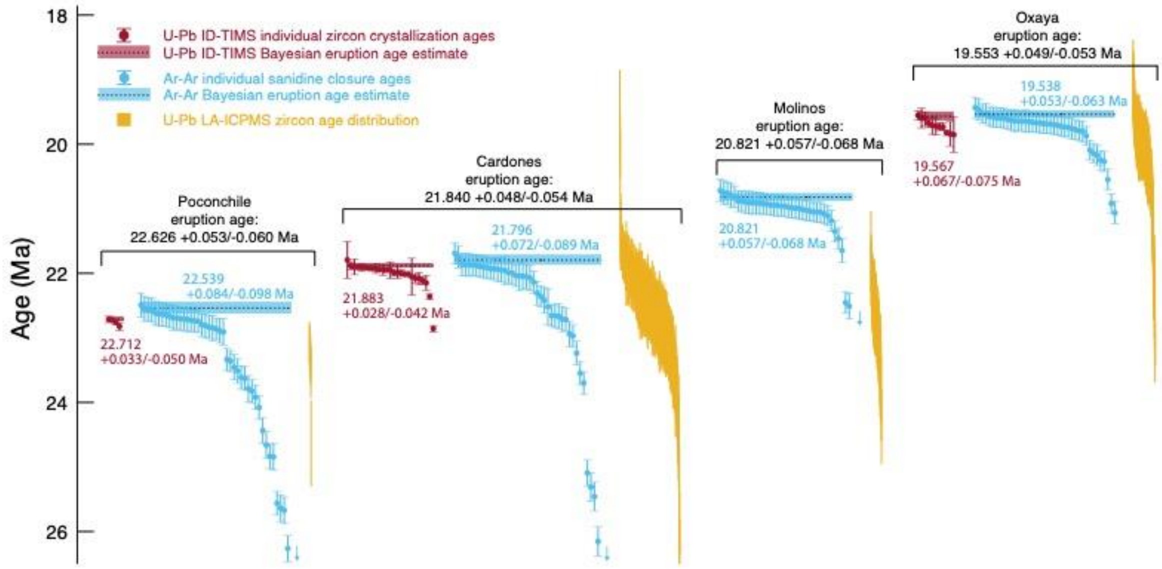

Figure 2. Geochronological data for the four ignimbrites of the Oxaya Formation. Four kinds of data are shown: U-Pb ages (CA-ID-TIMS) of individual euhedral zircons updated from van Zalinge et al.[27] using the Bayesian method[66,67]; $^{40}Ar/^{39}Ar$ ages of individual sanidine fragments; and U-Pb ages (LA-ICP-MS) of individual zircons. Our preferred eruption age comes from integration of the CA-ID-TIMS U-Pb ages of zircons and $^{40}Ar/^{39}Ar$ ages of sanidines. The data are ordered by age from left to right. Two-sigma analytical uncertainties are shown for individual sanidine and zircon ages; Bayesian eruption ages are reported with the 95% confidence interval (full external precision).

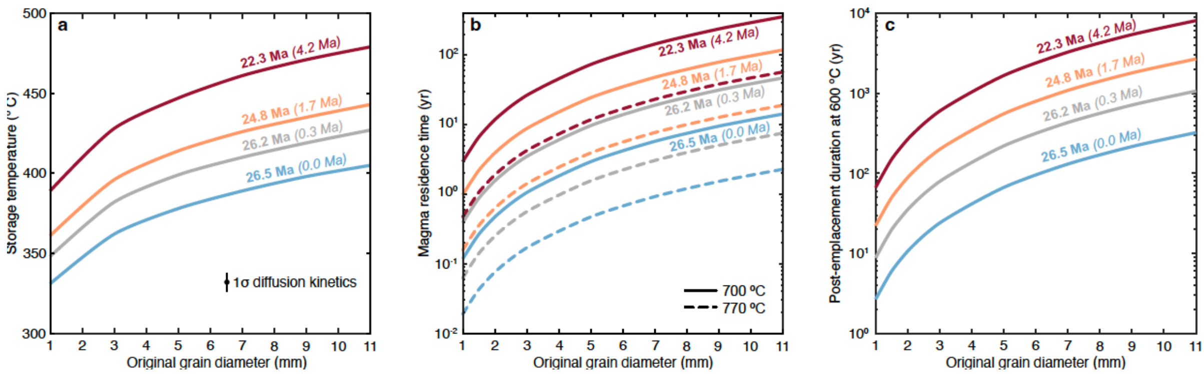

Figure 3. Models of the effects of (A) storage temperatures, (B) magma residence times, and (C) post-emplacement welding and cooling of ignimbrites on sanidine $^{40}Ar/^{39}Ar$ ages in the cores of sanidine crystals. We show model ages for crystal cores, where the core is defined as a volume at the center of the original crystal with a diameter 50% of the original crystal. We show $^{40}Ar/^{39}Ar$ ages of crystal cores for two reasons. First, we know that $^{40}Ar/^{39}Ar$ measurements were made on sanidine crystal fragments, and that grains were fragmented during mineral separation. Second, diffusive loss of ^{40}Ar causes rim-to-core age gradients; therefore crystal cores provide the oldest ages in our observed $^{40}Ar/^{39}Ar$ age distributions. For each set of models, we assume that sanidines crystallized at 26.5 Ma and that eruption occurred at 21.8 Ma. (A) Modeled sanidine core $^{40}Ar/^{39}Ar$ age as a function of original grain size and storage temperature. (B) Modeled sanidine core $^{40}Ar/^{39}Ar$ age as a function of original grain size and magma residence time, assuming no diffusive ^{40}Ar loss occurred prior to magma entrainment. Models are shown for two magma temperatures, 700 and 770ºC, based on geothermometry[29]. (C) Modelled sanidine core $^{40}Ar/^{39}Ar$ age at 600ºC, the maximum temperature during post-emplacement welding and cooling of the ignimbrites, assuming no diffusive ^{40}Ar loss during pre-eruption storage or magma residence.

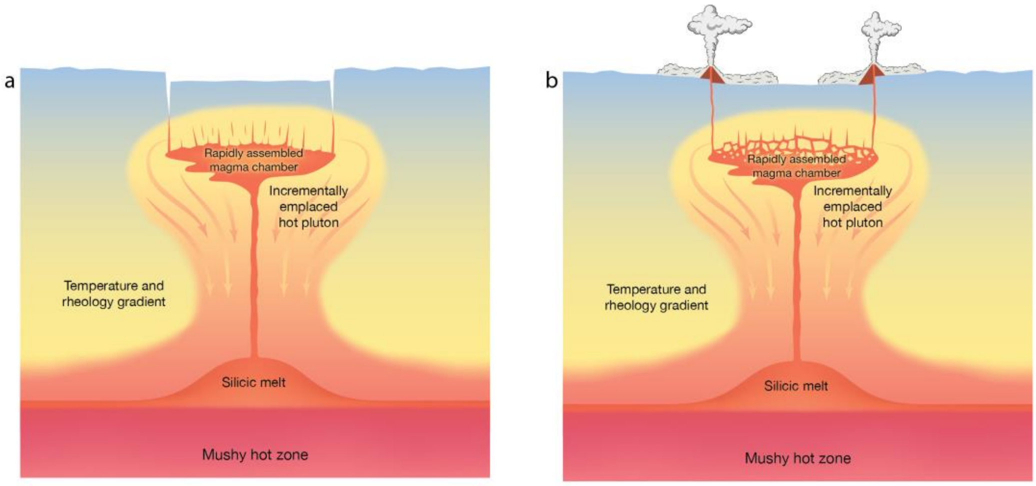

Figure 4. Conceptual model of a transcrustal magmatic system involving segregation of silicic melt from a middle to lower crustal hot zone, incipient Rayleigh Taylor instability and transfer to an upper crustal magma chamber by a dyke. Depiction is after the incubation period in which a large pluton system has been emplaced in the upper crust and hosts the development of the large magma chamber. In (a) emplacement of the shallow magma chamber is accompanied by deformation of co-genetic earlier plutonic rocks whereas in (b) the roof rocks are disrupted and incorporated into the erupting magma chamber.

Methods (words 2997)

Magma system Terminology

A transcrustal igneous system spans the mantle to the surface and includes magma chambers, igneous mush and fully solidified cognate igneous rocks below the solidus, as well as host rocks incorporated into the system by intrusive mechanisms. Mush is defined as a mixture of melt and crystals forming an interconnected framework in any proportions[8], while magma is sufficiently melt-rich that any crystals are suspended. Transition between mush and magma occurs over crystal contents of typically 50-60%. A magma reservoir is that part of the system containing melt. Mechanisms of forming large bodies of magma (ie. magma chambers)[8] include: incremental intrusion at flux rates sufficient to sustain high enough temperatures for magma formation[14]; segregation of evolved melts at the top of or within mushes[20,22,49]; amalgamation of smaller-scale melt-rich layers within mushes to form larger-volume magma bodies[24]; reheating of mush or fully solidified igneous rocks[50]; and fluxing of higher-temperature fluids transferred from hotter mafic magmas[51,52]. Super-eruptions are defined as eruptions of magnitude 8 or greater[53].

Geochronology

$^{40}Ar/^{39}Ar$ ages were obtained from sanidine phenocrysts. Pyroclasts were crushed in a jaw crusher, sieved, washed repeatedly in de-ionized water, before magnetically separated to isolate feldspar phenocrysts. The largest crystals without any inclusions were selected. Sanidine compositions within a single pumice are very homogenous except for some Ba-zonation[29].

Sanidine phenocrysts were leached in an ultrasonic bath in 5% HF for 5 minutes to remove adhering groundmass glass, before being rinsed three times in de-ionized water in an ultrasonic bath. Dried sanidines were passed through a magnetic separator at low speed and low angle of tilt, to remove crystals with mineral or melt inclusions. Samples were then hand-picked under a binocular microscope to eliminate those with inclusions and any visibly altered crystals. Sanidine crystals were harvested from individual pumice clasts and pumice fiamme from the Cardones and Molinos ignimbrites to avoid contamination with accidental crystals picked up during eruption. However, for the fine-grained Poconchile and Oxaya ignimbrites we isolated sanidines from bulk rock ignimbrite samples with very low lithic contents to minimize contamination. Many sanidines from the Oxaya Formation are rich in Ba or have Ba-rich growth zones, so we are confident that the sanidines are cognate with the magmatic system, an interpretation confirmed *a posteriori*. Our samples are typically ~2 mm in dimension but may be fragments of larger crystals as phenocrysts up to 11 mm are common[27, 29]. 50 individual crystals from each ignimbrite for laser fusion $^{40}Ar/^{39}Ar$ geochronology. Details of the samples and results are given in Table M1. Data tables are in supplementary materials. There is no link between age and composition with respect to K, Ca and Cl.

Pristine crystals were parcelled into Cu packets, or Al discs, stacked in glass vials and sealed in a large glass vial for irradiation. International standard Fish Canyon sanidine (FCs; with an age of 28.294 ± 0.0036 Ma) were used as fluence monitors for J-determination and packaged throughout the stack at known spacing (geometry) in between samples. Samples and standards were irradiated at the Cd-lined (CLICIT) facility of the Oregon State University (USA)

TRIGA reactor for 15.02 hours. Single irradiated crystals (*n*= 30 per sample) were fused with a CO_2 laser and isotope data were collected using a MAP 215-50 noble gas mass spectrometer[54].

Samples were analyzed in a single batch; backgrounds and mass discrimination measurements (via automated analysis of multiple air pipettes) specific to each batch were used to correct the data. Air pipettes were run (on average) after every 4 analyses. Backgrounds subtracted from ion beam measurements were arithmetic averages and standard deviations. Mass discrimination was based on a power law relationship[55] using the isotopic composition of atmospheric Ar[56] that has been independently confirmed[57]. Corrections for radioactive decay of ^{39}Ar and ^{37}Ar used published decay constants[58,59]. Ingrowth of ^{36}Ar from decay of ^{36}Cl was corrected using the $^{36}Cl/^{38}Cl$ production ratio and methods of Renne et al.[60] and was negligible.

The samples were analyzed by total fusion and step-heating with a CO_2 laser. The mass spectrometer is equipped with a Nier-type ion source. The MAP 215-50 data were collected using an analogue electron multiplier detector. Mass spectrometry utilized peak-hopping by magnetic field switching for 10 cycles.

Ages were computed from the blank-, discrimination- and decay-corrected Ar isotope data after correction for interfering isotopes based on the following production ratios, determined from fluorite and Fe-doped $KAlSiO_4$ glass: $(^{36}Ar/^{37}Ar)_{Ca} = (2.650 \pm 0.022) \times 10^{-4}$; $(^{38}Ar/^{37}Ar)_{Ca} = (1.96 \pm 0.08) \times 10^{-5}$; $(^{39}Ar/^{37}Ar)_{Ca} = (6.95 \pm 0.09) \times 10^{-4}$; $(^{40}Ar/^{39}Ar)_{K} = (7.3 \pm 0.9) \times 10^{-4}$;

$(^{38}Ar/^{39}Ar)_K$ = $(1.215 \pm 0.003) \times 10^{-2}$; $(^{37}Ar/^{39}Ar)_K$ = $(2.24 \pm 0.16) \times 10^{-4}$, as determined previously for this reactor in the same irradiation conditions[61]. Ages and their uncertainties are based on methods of Renne et al.[62], calibration of the decay constant[63] and the FCs optimization age. The optimization-modeled age has accurate quantifiable uncertainties. The reason for this preference over the astronomically tuned FCs ages[64] is that astronomical calibration has unknown uncertainty and confidence intervals and uses best guess 'assumptions' to constrain, for example, phase relationships between insolation and climate.

For age comparisons, contributions from sources of systematic uncertainty (i.e., uncertainties in $^{40}Ar/^{40}K$ of the standard and ^{40}K decay constants) are neglected and only analytical uncertainties (referred to as "analytical precision) in isotope measurements of samples and standards are included[65]. In this study analytical uncertainties include contributions from uncertainties in the interference corrections which have variable effects due to slight variations in sample composition.

Information on samples and geochrononological data are summarized in Table ED1. The individual geochronological data of zircons and sanidines are provided in Tables ED2 and ED3.

Zircon ages of three of the Oxaya ignimbrites have been previously presented[27]. The previous study determined eruption ages by single-crystal zircon U-Pb CA-ID-TIMS $^{206}Pb/^{238}U$ analyses of high aspect ratio zircons lacking any complex crystal shapes and evidence of older cores. In this study zircons with complex resorbed cores that were previously excluded from the U–Pb CA-ID-TIMS $^{206}Pb/^{238}U$ analyses, were analysed at the Geochronology & Tracers Facility, British Geological Survey (GTF-BGS) using a Nu Instruments, Nu Plasma HR, multi-collector inductively coupled plasma mass spectrometer (MC-ICP-MS). The Nu Plasma HR was operated in static mode, with simultaneous measurement of isotopes on either a Faraday detector or an ETP secondary electron multiplier (see Table M2 below). Ages determined by LA-ICP-MS from inherited zircons (Figure 2) reveal highly dispersed age spectra (MSWD >7 for samples with >50 analyses).

ExH	H6	H4	H3	H2	H1	Ax	L1	L2	IC0	IC1	L3	IC2	L4	L5*1
^{238}U	^{235}U	–	–	–	–	–	–	–	^{207}Pb	^{206}Pb	–	^{204}Pb ^{204}Hg	–	^{202}Hg
		Detectors not in use												

Table M2: Configuration of the Nu Plasma HR 'Zircon' block used for U-Pb geochronology at GTF-BGS. *1 measured to allow for the correction of ^{204}Hg on ^{204}Pb. H denotes high mass Faraday collectors, L denotes low mass Faraday collectors and IC denotes ion counter detectors.

Laser sampling used a New Wave Research 193nm laser ablation system, incorporating an in-house designed, low-volume sample cell with an ablation volume of ca. 3-4 cm^3, which, when combined with ~1 m tubing to the plasma torch, leads to a signal washout time of ~ 1 second. Ablation parameters were: 35 µm static spot, run at a repetition rate of 10Hz, with a fluence of ~2.2 J/cm^2. Samples were ablated for 30 seconds with a 15 second washout/laser warm-up period between each analyses.

Data were acquired using the time-resolved analysis function of the Nu HR's software, and processed using Iolite; a software package specifically designed to handle the large volumes of data produced by LA-ICP-MS. Lolite correct data using the 'standard-sample-bracketing' technique, which applies a normalisation factor (measured/known) to the data for the ^{207}Pb/^{206}Pb and ^{206}Pb/^{238}U of a primary zircon reference material (91500; 1062 ± 0.4 Ma), analysed at regular intervals during each session. Two other zircon reference materials (GJ1 and Mud Tank, 602 ± 1Ma and 732 ± 5 Ma, respectively) were analysed during each session, to check for accuracy and precision.

Propagated uncertainties were produced by Iolite and reflect the quadratic combination of the internal uncertainty, (i.e. the reproducibility of the measured ratios) with the external uncertainty (i.e. the reproducibility of the bracketing reference material). Components relating to the systematic uncertainty of the method (i.e. age uncertainty of primary reference material, decay constant uncertainties and long-term variance of secondary reference material) are quadratically added, post Iolite.

Dispersed ^{40}Ar/^{39}Ar and the previously published CA-ID-TIMS U-Pb age distributions (Figure 2) preclude calculation of a weighted mean, leading us to adopt a Bayesian approach to eruption age estimation based on the algorithm of Keller et al.[66]. Bayesian eruption age estimation requires a prior estimate of the *relative age distribution* of crystallization (zircon) or apparent closure (sanidine) ages before eruption, which was estimated by bootstrapping[67].

Incorporating all available ^{40}Ar/^{39}Ar age distributions that feature well-resolved pre-eruptive heterogeneity, bootstrapping by kernel density estimation reveals (Figure S1) a consistent, exponential form of the relative closure age distribution. This exponential form suggests an underlying survivorship process (e.g. potentially consistent with geologic processes ranging from partial degassing of sanidine antecrysts to pre-eruptive Ar accumulated in a cold-storage regime). For excess Ar the observed continuum of ages would not be expected. Using this bootstrapped age distribution, the resulting eruption age estimates based on $^{40}Ar/^{39}Ar$ sanidine ages for the Cardones are indistinguishable within uncertainty from those based on U-Pb CA-ID-TIMS zircon crystallization ages (Table MD1), whereas the $^{40}Ar/^{39}Ar$ sanidine ages for Poconchile and Oxaya ignimbrites are just beyond uncertainty of each other. To account for this we calculate an integrated $^{40}Ar/^{39}Ar$ and U-Pb age that accounts for the scatter.

We re-calculated the previous CA-ID-TIMS zircon ages[27] using the Bayesian method, Incorporating constraints from both sanidine and zircon eruption age estimates, we estimated repose intervals between eruptions (Figure S2) using the superposition algorithm of Keller[66].

We first estimated empirically the form of the *relative closure distribution,* analogous to the *relative crystallization distribution* of Keller et al.[67] using a method equivalent to the "boostrapping" approach[68]. The results (Figure S1) revealed a characteristic form of the closure distribution featuring a nearly exponential decrease in probability density with increasing time prior to eruption. The consistency and reproducibility of this form, to first order, between all available well-resolved single-crystal volcanic sanidine $^{40}Ar/^{39}Ar$ age distributions (both from these Andean ignimbrites and the Mesa Falls Tuff[68]) suggests that this exponential form may be underlain by a consistent physical process. A survivorship process wherein, for example, each sanidine has some finite probability of being reset by reheating in any given pre-eruptive time interval provides one simple mechanism for producing such a trend.

We applied the Markov chain Monte Carlo eruption age estimation algorithm in the Chron.jl software package[66] to each ignimbrite, using a half-Normal relative crystallization distribution for all CA-ID-TIMS zircon ages, and our previously determined exponential relative closure distribution for all sanidine ^{40}Ar/^{39}Ar ages (Figure S2). Systematic uncertainties were propagated using the “optimization intercalibration" the constants of Renne et al.[63] for ^{40}Ar/^{39}Ar ages, and the decay constants of Jaffey et al.[69] along with the effective systematic uncertainty of the EarthTime tracer[70,71] for U-Pb TIMS ages. Finally, to estimate repose intervals between each ignimbrite (Figure S2), we used Chron.jl to run a second “stratigraphic” MCMC model, combining both the new eruption age estimates and relative age constraints provided by the stratigraphy. Table M1 shows all model outputs.

Diffusion modeling

Argon diffusion calculations were carried out using analytical solutions for simultaneous production and diffusion[72,73]. These solutions, which involve two infinite series, typically converge with less than 20 partial sums. We use measured argon diffusion kinetics for Fish Canyon sanidine[74]. We assume that all sanidine crystals form at 26.5 Ma andreside at a constant temperature until 21.8 Ma (the approximate eruption age of Cardones). To estimate magma residence times, we assume that no argon diffusion occurs during cold storage (i.e., that ^{40}Ar concentration profiles in sanidine crystals were uniform at the beginning of magma residence). Because some prior diffusive rounding of the ^{40}Ar concentration profiles likely occurred during cold storage, our estimates of magma residence times should be considered minima.

Uncertainties in cold storage temperatures due to uncertainties in argon diffusion kinetics are fairly invariant and range from $\pm$ 5 to $\pm$ 6 ºC (1σ), with the largest uncertainties corresponding to small grain sizes and low degrees of fractional argon loss (i.e., older $^{40}Ar/^{39}Ar$ ages). Because magma residence times range over a few orders of magnitude, absolute uncertainties in magma residence times due to uncertainties in argon diffusion kinetics also range over a few orders of magnitude. Generally, magma residence time uncertainty increases with increasing degree of fractional argon loss (i.e., younger $^{40}Ar/^{39}Ar$ ages), increasing grain size, and decreasing magma residence temperature. Relative uncertainties in magma residence times, on the other hand, are essentially invariant with grain size or degree of fractional loss, and are ~7% for residence temperatures of 700 ºC and ~3% for residence temperatures of 770 ºC. For example, for an 11 mm-diameter sanidine grain that experienced 96% fractional loss (i.e., has an $^{40}Ar/^{39}Ar$ age of 22 Ma), the residence time at 700 ºC is 356 $\pm$ 25 years, while the residence time at 770 ºC is 57 $\pm$ 2 years.

Magma transport modelling

We apply here an experimentally verified model for development of buoyancy induced instability for a growing melt layer beneath a layer of much greater viscosity[23]. Here a silicic melt layer extracted from an underlying mush accumulates beneath hot upper crust (Figure 4). The fastest-growing wavelength of the Rayleigh Taylor (RT) instability in the case of an unconfined layer is given by:

$$\lambda = 9.058\ (\dot{h} / \Delta\rho\, g)^{1/2}\, \mu_m^{1/6}\, \mu_c^{2/3} \qquad \text{(M1)}$$

where $\dot{h}$ is the growth rate of the unstable layer, g is gravity, $\Delta\rho$ is the density difference between melt and overlying crust, μ_m is the viscosity of the silicic melt layer, and μ_c is the viscosity of overlying hot just sub-solidus crust. Representative values are $\Delta\rho$ = 300 kg/m^3, μ_m = 10^5 Pa s, and μ_c = 10^{19} Pa s[43]. We take $\dot{h}$ values of 1 mm and 5 mm/year based on models of reactive flow related to basalt underplating[21] resulting in λ values of 600 and 1400 km. Although approximate these calculations show that the fastest growing wavelength is much larger than the width of zones of magma generation beneath batholiths, taken here to be typically in the range 30 to 50 km. Thus we have applied the theory for confined instability growth[23] for $\mu_m << \mu_c$ to calculate a characteristic time scales for instability:

$$\tau = (6\pi\mu_c)/(\Delta\rho\ g\ D) \qquad \text{(M2)}$$

with D, the width (diameter) of the layer. During experiments described in Seropian et al.[23] we observed from 16 experiments covering a wide range of material properties (analogue melt layer thicknesses, μ_c and $\Delta\rho$) that the time it takes an instability to transform into a detached diapir was about 4 greater than τ, leading to:

$$\tau_d = (24\pi\mu_c)/(\Delta\rho\ g\ D), \qquad \text{(M3)}$$

which we applied in the main text.

One possibility is that the RT instability grows to form a diapir which traverses the intervening plutonic crust. However, magma transport by diapirism is too slow to explain the rapid assembly of magma chambers prior to ignimbrite eruptions: we estimate using equation 8 in

Burov et al.[46] that a 1000 km^3 diapir with $\Delta\rho$ = 300 kg/m^3 takes ~ 10^5 years to rise 10 km in a crust with an effective viscosity of 10^{19} Pa s. This simplified calculation does not consider heat loss from the diapir, which locally reduces the viscosity of the surroundings[45], which in turn enables somewhat faster ascent and could help assimilate older plutonic material into the diapir as it ascends. This mechanism could explain the spectrum of zircon ages but is not consistent with abundant old sanidines. Thus dyke transport[47] provides an attractive mechanism to enable fast magma chamber assembly.

In our conceptual model (Figure 4) a conduit (dyke or cylinder) is formed that allows an exchange flow[48] between the middle crustal melt layer and an upper crustal region in which a magma chamber forms. Here we envisage that upward flow of magma along the conduit is balanced by the downward subsidence of the crust. We are interested in the case where the cross-sectional area of the magma conduit is much less than the area of crust flowing downwards ($A_m << A_c$) and the magma is much less viscous than the crust ($\mu_m << \mu_c$). In this scenario the average speed of the crust downward (U_c) is less than the average magma flow speed up the conduit: $U_c \approx (A_m / A_c) U_m$ by many orders of magnitude. To develop a very simple model we represent the subsiding crust as a large cylinder of radius R and the conduit as a small cylinder of radius r; note that for a dyke with a length 1000 times its width, its width is approximately a quarter of the radius r of a cylindrical conduit that would accommodate the same flux. Due to the low crust velocity and the large viscosity contrast, the upward flow of magma is well approximated by flow through a cylinder with solid walls (Poiseuille flow):

$$Q = [\pi r^4 \Delta\rho g]/8\mu_m \qquad \text{(M4)}$$

where Q is the magma flux (volume/time) through the conduit. Approximating the downward flow as Poiseuille flow with radius R also with flux Q, results in the following relationship:

$$r = (\mu_m/\mu_c)^{1/4} R \qquad \text{(M5)}$$

We have applied equations to make the calculations (Table 1). The difference between an exchange flow along a cylinder and a dyke is a matter of geometry with viscous friction being a factor of a few greater in a dyke with the same cross-sectional area as a cylinder. The length of the dyke is an additional factor in governing friction and different choices could be made, but would have a minor effect on calculated magma fluxes. Thus the essential elements of exchange flow are captured by a cylindrical conduit. Even for a cylindrical geometry our approximate calculations are intended only to illustrate the feasibility of the crust subsiding slowly over a large area allowing an exchange flow with relatively fast ascent of magma from the mid- to the upper crust.

Methods References

49. Jackson, M. D., Cheadle, M. J. & Atherton, M. P. Quantitative modeling of granitic melt generation and segregation in the continental crust. Journal of Geophysical Research 108, 2332-2353(2003).

50. Huppert, H.E. & Sparks, R.S.J. The generation of granite by intrusion of basalt into the continental crust. Journal of Petrology 29, 599-624 (1988).

51. Bachmann, O. & Bergantz, G. W. Gas percolation in upper crustal silicic crystal mushes as a mechanism for upward heat advection and rejuvenation of near-solidus magma bodies. Journal of Volcanology and Geothermal Research 149, 85-102 (2006).

52. Huber, C., Bachmann, O. & Manga, M. Two Competing Effects of Volatiles on Heat Transfer in Crystal-rich Magmas: Thermal Insulation vs Defrosting. Journal of Petrology 51, 847-867 (2010).

53. Mason, B., Pyle, D. & Oppenheimer, C. The size and frequency of the largest explosive eruptions on earth. Bulletin of Volcanology 66, 735-748 (2004).

54. Mark, D.F., Petraglia, M., V.C. Smith, Morgan, L.E., Barfod, D.N., Ellis, B.S. N.J.Pearce, Pal, J.N. & Korisettar, R. A high-precision $^{40}Ar/^{39}Ar$ age for the Young Toba Tuff and dating of ultra-distal tephra: forcing of Quaternary climate and implications for hominin occupation of India. Quaternary Geochronology 21, 90-103 (2014).

55. Renne, P.R. Cassata, W.S. & Morgan, L.E. The isotopic composition of atmospheric argon and $^{40}Ar/^{39}Ar$ geochronology: time for a change? Quaternary Geochronology 4, 288-298 (2009).

56. Lee, J.Y. Marti, K., J.P. Severinghaus, J.P., Kawamura, K., Yoo, H.S., Lee, J.B. & Kim, J.S. A redetermination of the isotopic abundances of atmospheric Ar. Geochimica et Cosmochimica Acta 70, 4507-4512 (2006)

57. Mark, D.F., Stuart, F.M., & de Podesta, M. New high-precision measurements of the isotopic composition of atmospheric argon. Geochimica et Cosmochimica Acta 75, 7494-7501 (2011).

58. Stoenner, R.W., Schaeffer, O.A. & Katcoff, S. Half-lives of argon-37, argon-39, and argon-42. Science 148, 1325- 132 (1965).

59. Renne, P.R. & Norman, E.B. Determination of the half-life of ^{37}Ar by mass spectrometry. Physics Reviews C 63, 047302 (2001).

60. Renne, P.R., Sharp, Z.D. & Heizler, M.T. Cl-derived argon isotope production in the CLICIT facility of OSTR reactor and the effects of the Cl-correction in ^{40}Ar/^{39}Ar geochronology. Chemical Geology 255. 463-466 (2008).

61. Renne P.R. Some footnotes to the optimization-based calibration of the ^{40}Ar/^{39}Ar system. Geological Society London Special Publication 378, 21-31 (2014).

62. Renne, P.R., Mundil, R., Balco, G., Min, K. & Ludwig , K.R. Joint determination of 40K decay constants and ^{40}Ar∗/^{40}K for the Fish Canyon sanidine standard, and improved accuracy for ^{40}Ar/^{39}Ar geochronology. Geochimica et Cosmochimica. Acta 74, 5349-5367 (2010).

63. Renne, P.R., Mundil, R., Balco, G., Min, K., Ludwig K.R. Response to the comment by W. H. Schwarz et al. on "Joint determination of ^{40}K decay constants and ^{40}Ar∗/^{40}K for the Fish Canyon sanidine standard, and improved accuracy for ^{40}Ar/^{39}Ar geochronology. Geochimica et.Cosmochimica Acta 75, 5097-5100 (2011).

64. Kuiper, K.F., Deino, A., F.J. Hilgen, F.J., Krijgsman, Renne, P.R. & Wijbrans, J.R. Synchronizing rock clocks of Earth history. Science 320, 500-504 (2008).

65. Mark, D.F., Renne, P.R. Dymock, R.C., Smith, V.C., Simon, J.I., Morgan, L.E. Saff, R.A., Ellis, B.S. & Pearce, N.J.G. High precision 40Ar/39Ar dating of Pleistocene tuffs and temporal anchoring of the Matuyama-Brunhes Boundary. Quaternary Geochronology 39, 1-23 (2017).

66. Keller, C.B. Chron.jl: A Bayesian framework for integrated eruption age and age-depth modelling. https://doi.org/10.17605/osf.io/TQX3F (2018).

67. Keller, C. B., Schoene, B. & Samperton, K. M. A stochastic sampling approach to zircon eruption age interpretation. Geochemical Perspectives Letters 8, 31–35 (2018).

68. Ellis, B.S., Mark, D.F., Troch J., Bachmann, O., Guillong, M, Kent, A.J.R. & von Quadt, A. Split-grain ^{40}Ar/^{39}Ar dating: Integrating temporal and geochemical data from crystal cargoes. Chemical Geology 457, 15-23 (2017).

69. Jaffey, A.H., Flynn, K.F., Glendenin, L.E., Bentley, W.C. & Essling, A.M. Precision Measurement of Half-Lives and Specific Activities of ^{235}U and ^{238}U. Physics Reviews C 4, 1889 (1971).

70. Condon, D.J., Schoene, B., McLean, N.M., Bowring, S.A. & Parrish, R.R. Metrology and traceability of U–Pb isotope dilution geochronology (EARTHTIME Tracer Calibration Part I). Geochimica et Cosmochimica Acta 164, 464-480 (2015).

71. McLean, N.M. , Condon D.J., Schoene, B. & Bowring, S.A. Evaluating uncertainties in the calibration of isotopic reference materials and multi-element isotopic tracers (EARTHTIME Tracer Calibration Part II). Geochimica et Cosmochimica Acta 164, 481-502 (2015).

72. Wolf, R. A., Farley, K. A. & Kass, D. M. Modeling of the temperature sensitivity of the apatite (U–Th)/He thermochronometer. Chemical Geology 148, 105–114 (1998).

73. McDougall, I., & Harrison, T. M. Geochronology and Thermochronology by the ^{40}Ar/^{39}Ar Method. (Oxford University Press on Demand, 1999).

74. Cassata, W. S. & Renne, P. R. Systematic variations of argon diffusion in feldspars and implications for thermochronometry. Geochimica et Cosmochimica Acta 112, 251–287 (2013).

Acknowledgements

This project was funded by BHP supporting the PhD of Marit van Zalinge. BHP have given permission to publish. Kari Cooper and an anonymous reviewer are thanked for their supportive and careful reviews. Zircon and sanidine analyses were supported by Natural Environment Research Council Isotope Geosciences Facilities Steering Committee grant IP-1466-1114 and Royal Society Research Grant RG140683 to FJC. Dan Condon is thanked for his help with the analyses of inherited zircons. NERC are thanked for ongoing funding of the National Environmental Isotope Facility. RSJS acknowledges support of a Leverhulme Trust Emeritus Fellowship.

Author contributions.

Van Zalinge carried out field work, collected the samples and prepared them for geochronological analyses. Mark conducted the $^{40}Ar/^{39}Ar$ analyses at the East Kilbride laboratories. Keller and Mark applied a Bayesian model to interpret the geochronological data. Mark and Sparks integrated and interpreted the geochronology and developed the scientific narrative. Tremblay contributed argon diffusion modeling to estimate storage temperatures and magma residence times for sanidine crystals. Rust analysed RT experiment data for the diapir detachment timescale. Rust and Sparks developed the exchange flow models for magma transport. Sparks and Mark led drafting the article and all authors contributed to the writing. Cooper and Sparks supervised PhD student Van Zalinge.